Geophys. J. Int. (1994) **116,** 637–654

The Somalia plate and the East African Rift System: present-day kinematics

F. Jestin,[1] P. Huchon[1] and J. M. Gaulier[2]

[1]*INSU/CNRS, URA* 1316, *Laboratoire de Géologie, Ecole Normale Supérieure,* 24 *rue Lhomond,* 75231 *Paris Cedex* 05, *France*
[2]*Institut Français du Pétrole,* 1 & 4 *rue de Bois-Préau,* 92506 *Rueil-Malmaison, France*

Accepted 1993 July 28. Received 1993 July 22; in original form 1992 October 6

SUMMARY

The motion of the Somalia plate relative to the Nubia (Africa), Arabia and Antarctica plates is re-evaluated using a new inversion method based on a Monte Carlo technique and a least absolute value misfit criterion. A subset of the NUVEL 1 data set, with additional data along the Levant Fault and in the Red Sea is used. The results confirm that the motion of Arabia with respect to Africa is significantly different from the motion relative to Somalia. It is further shown that the data along the SW Indian Ridge are compatible with a pole of relative motion between Africa and Somalia located close to the hypothetical diffuse triple junction between the ridge and the East African Rift. The resulting Africa–Somalia motion is then compatible with the geological structures and seismological data along the East African Rift system. Assuming a separate Somalia plate thus solves kinematic and geological problems around the Afar triple junction and along the East African Rift.

Key words: Africa, Antarctic, inversion, Red Sea, rifts, tectonics, triple junction.

INTRODUCTION

The existence of a plate boundary which separates the western Africa (AFRI) (Nubia) plate from the Somalia (SOMA) plate is substantiated by seismicity (Fig. 1) as well as by a complex set of extensional structures named the east African Rift system (EAR). The EAR, first described in 1921 by Gregory, constitutes, with the Red Sea and the Gulf of Aden, the Afar triple junction, the only emerged RRR type triple junction (McKenzie & Morgan 1969). Although regional kinematic models (McKenzie, Davies & Molnar 1970; Le Pichon & Francheteau 1978; Joffe & Garfunkel 1987) propose kinematic solutions around the Afar triple junction, global instantaneous kinematic models such as RM2 (Minster & Jordan 1978) and NUVEL 1 (DeMets *et al.* 1990) do not include the SOMA plate. Although they predict east–west extension across the EAR, regional kinematic models are not fully satisfactory as they do not ensure closure of the global plate circuit. The main purpose of this paper is thus to explore the kinematic solutions for the motion of the SOMA plate with respect to the surrounding AFRI (Nubia), Arabia (ARAB) and Antarctica (ANTA) plates which are simultaneously consistent with geological and geophysical data around the Afar triple junction (see, for example, Jestin & Huchon, 1992) and with the NUVEL 1 global model.

The only global model which includes the SOMA plate and predicts east–west extension along the EAR is that of Chase (1978). Stein & Gordon (1984) also noted that 'a model with an undivided Indian plate but separate West African and Somalian plates fits the data significantly better than a model with an undivided African plate'. In their description of NUVEL 1, DeMets *et al.* (1990) stated that 'global models with distinct Nubian and Somalian plates predicted slow (~3 mm yr $^{-1}$), right-lateral slip along the East African Rift. Because this unsuccessful model disagrees with the observed E–W extension in the East African Rift, we treat Africa as a single plate, and omit both azimuths and spreading rates from the Red Sea'. Apparently, DeMets *et al.* (1990) encountered the same problem as Minster & Jordan (1978), who briefly describe a model including Somalia which predicted convergence rather than extension along the EAR. For that reason, the SOMA plate was not included in RM2. Forsyth (1975), Norton (1976) and Joffe & Garfunkel (1987) also derived AFRI–SOMA rotation parameters that imply convergence along the EAR [only in its southern part in the Joffe & Garfunkel (1987) model]. As noted by DeMets *et al.* (1990), simply considering Red Sea spreading rates is not sufficient to lead to a global model consistent with the EAR. This paper shows that this problem disappears when the Levant Fault system is taken into account within a regional kinematic model that is later shown to be compatible with NUVEL 1. In this paper particular attention is paid to the constraints on the

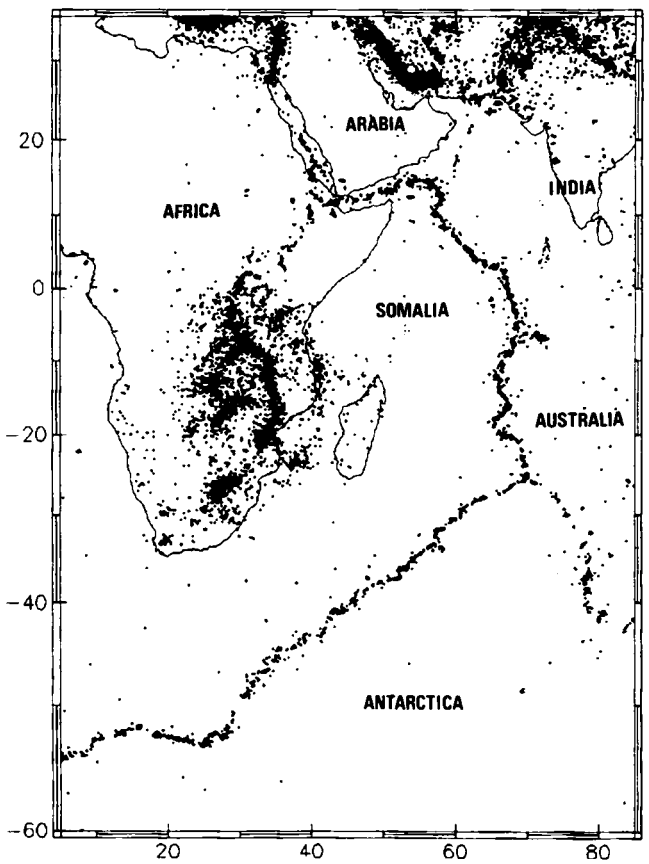

Figure 1. Global seismicity (from ISC Bulletins) around the SOMA plate. Note the diffuse pattern of seismicity along the East African Rift.

ARAB–AFRI motion, following the analyses of Joffe & Garfunkel (1987) and Le Pichon & Gaulier (1988).

Another approach to the problem of AFRI–SOMA relative plate motion comes from considering data along the south-west Indian Ridge (SWIR). Based on statistical considerations, DeMets, Gordon & Argus (1988) reached the conclusion that the AFRI–SOMA relative plate motion is negligible near the SWIR. In other words, all the data along this ridge can be fitted satisfactorily with a single Euler vector. Although this is true, it does not mean that the EAR should not be considered as a plate boundary. It may also result from an AFRI–SOMA pole of rotation located close to the triple junction, as is shown later.

It is first confirmed that the relative motions in the Red Sea and Gulf of Aden cannot be explained by a single African plate (AFRI + SOMA). It is further shown that although data along the SWIR can be explained with a single rotation vector, they can also fit, within the data uncertainties, with a three plate system (AFRI–SOMA–ANTA). Finally, it is shown that a simultaneous inversion of all the data along the Red Sea, the Gulf of Aden and the SWIR leads to an AFRI–SOMA rotation pole which is indeed located close to the diffuse AFRI–SOMA–ANTA triple junction, and is in agreement with the observed deformation pattern along the EAR.

A data set (Table 1) similar to a subset of that used in NUVEL 1 (DeMets *et al.* 1990) and in the papers by DeMets *et al.* (1988), Gordon & DeMets (1989) and Gordon, DeMets & Argus (1990) was used. Data were added where the previous models did not use any constraint, especially in the Red Sea, along the Levant Fault system and along the western part of the SWIR. Additional slip vectors were taken from centroid moment tensor (CMT) catalogues. For additional spreading rates in the Red Sea, the time-scale of Harland *et al.* (1982) was used to be consistent with NUVEL 1. A different source of data was used for transform fault azimuths in the Gulf of Aden (see the following).

OUTLINE OF THE INVERSION TECHNIQUE

The first inversion method to compute an instantaneous kinematic model was proposed by Chase (1972). Minster & Jordan (1978) and DeMets *et al.* (1990) have used similar techniques. Their method consists in linearizing the problem about an *a priori* model and in minimizing the sum of misfits in the least-squares sense (or L2 norm). Another approach to the problem is that used by Le Pichon (1968) to obtain the first global kinematic model. Instead of a direct inversion, a systematic search was applied on a regular grid in the parameter space. However, this method is expensive if the data set and the number of plates are large. Instead, a more efficient random search, such as the Monte Carlo method, is widely used in inversion problems. In this paper a new inversion method based on this technique is used.

To ensure the stability and robustness of the solution, the least absolute value criterion (L1 norm) is used instead of the usual least-squares criterion (L2 norm). Stability is defined as the sensitivity of the solution to small random errors in the data set. If the *a priori* information is correctly introduced, stability is generally ensured. Robustness is defined as the sensitivity to a few large errors in the data set. The hypothesis of Gaussian errors on the data, made by most workers (Chase 1972, 1978; Minster *et al* 1974; Minster & Jordan 1978; DeMets *et al* 1990) is not robust (Tarantola 1987). On the contrary, the hypothesis of exponential errors is robust. However, in absence of outliers in the data set, the results obtained when using the L1 or L2 criterion are very similar.

Formulation

Defining a probability density over a space of discrete parameters is the most general way to describe the information available about these parameters (Tarantola 1987). Moreover, the conjunction of two states of information is simply the product of the associated probability densities (Tarantola & Valette 1982). Therefore the most general way to define the solution of an inverse problem is to consider the solution as the intersection of two states of information, on the data and on the model (Tarantola 1987). In the following, the results presented by Tarantola (1987) are used directly, where it is shown that if it is known how to solve the direct problem

$$\mathbf{d} = f(\mathbf{m}) \tag{1}$$

where $\mathbf{d}$ and $\mathbf{m}$ represent the data set and the model parameters, respectively, the solution of the inverse

Table 1. Data used in this study.

Lat. °N	Lon. °E	Datum	σ	Model	M.dir.	Reference
Arabia-Africa: Spreading rates						
30.37	35.27	0.85	0.15	0.82	15	Garfunkel et al. (1981)
23.17	37.25	1.40	0.20	1.21	47	Izzeldin (1987)
18.79	39.57	1.70	0.20	1.58	47	Izzeldin (1987)
Arabia-Africa: Transform azimuths						
32.91	35.62	1	5	1		Garfunkel et al. (1981)
32.50	35.58	3	5	4		Garfunkel et al. (1981)
32.33	35.58	5	5	5		Garfunkel et al. (1981)
32.00	35.55	6	5	7		Garfunkel et al. (1981)
31.83	35.52	9	5	8		Garfunkel et al. (1981)
30.58	35.33	14	5	14		Garfunkel et al. (1981)
30.37	35.27	15	5	16		Garfunkel et al. (1981)
30.25	35.23	19	10	16		Garfunkel et al. (1981)
29.75	35.05	22	10	19		Garfunkel et al. (1981)
22.45	37.80	52	10	42		Izzeldin (1989)
19.90	38.61	50	10	47		Izzeldin (1989)
19.72	38.69	49	10	47		Izzeldin (1989)
19.47	38.88	48	10	47		Izzeldin (1989)
Arabia-Africa: Slip vectors						
31.24	35.46	21	20	11		CMT 4.23.79
19.50	38.80	50	15	47		Huang & Salomon (1987)
Arabia-Somalia: Spreading rates						
13.50	57.50	2.40	0.40	2.62	32	*Cochran (1981)
13.70	57.30	2.50	0.40	2.60	32	*Cochran (1981)
13.90	57.00	2.50	0.40	2.58	32	*Cochran (1981)
14.50	56.80	2.40	0.30	2.54	32	*Cochran (1981)
14.60	56.40	2.40	0.30	2.52	32	*Cochran (1981)
14.70	55.90	2.40	0.30	2.43	10	*Cochran (1981)
14.90	55.60	2.35	0.30	2.46	17	*Laughton et al. (1970)
14.80	54.80	2.30	0.30	2.42	17	*Laughton et al. (1970)
14.41	53.60	2.40	0.30	2.35	17	*Laughton et al. (1970)
13.20	51.00	1.90	0.40	2.24	22	*Cochran (1981)
13.40	50.90	2.10	0.40	2.22	22	*Laughton et al. (1970)
13.50	50.70	2.10	0.30	2.21	22	*Laughton et al. (1970)
13.40	50.40	2.15	0.30	2.18	20	*Tamsett & Girdler (1982)
12.15	45.85	1.50	0.40	1.80	10	*Girdler et al. (1980)
12.15	45.65	1.85	0.25	1.78	10	*Girdler et al. (1980)
12.10	45.55	1.60	0.30	1.78	10	*Tamsett & Girdler (1982)
12.08	45.47	1.85	0.25	1.77	10	*Girdler et al. (1980)
12.05	45.25	1.75	0.25	1.76	10	*Girdler et al. (1980)
12.05	45.17	1.65	0.25	1.75	10	*Girdler et al. (1980)
12.10	45.10	1.65	0.25	1.75	10	*Girdler et al. (1980)
12.10	44.92	1.65	0.25	1.73	10	*Girdler et al. (1980)
12.15	44.81	1.60	0.30	1.73	10	*Girdler et al. (1980)
12.05	44.59	1.55	0.25	1.63	5	*Girdler et al. (1980)
12.08	44.50	1.55	0.25	1.62	5	*Girdler et al. (1980)
12.05	44.29	1.65	0.25	1.61	5	*Girdler et al. (1980)
Arabia-Somalia: Transform azimuths						
12.92	57.94	25	10	26		Cochran (1981)
13.38	57.66	23	10	25		Cochran (1981)
13.78	57.26	25	10	25		Cochran (1981)
14.00	56.91	26	10	25		Cochran (1981)
14.20	56.66	30	10	25		Cochran (1981)
14.63	56.12	24	10	24		Cochran (1981)
14.70	55.58	21	10	24		Cochran (1981)
14.80	55.08	21	10	24		Cochran (1981)
14.80	54.43	22	10	25		Cochran (1981)
14.59	53.88	25	10	25		Cochran (1981)
14.75	52.08	28	5	26		Cochran (1981)
13.90	51.70	26	5	27		*DeMets et al. (1990)
13.06	51.20	29	5	29		Cochran (1981)
13.28	50.51	31	10	29		Cochran (1981)
13.16	50.22	36	10	30		Cochran (1981)
13.22	49.64	31	10	30		Cochran (1981)
12.85	48.83	33	10	31		Cochran (1981)
12.70	48.40	32	10	32		Cochran (1981)
12.60	48.10	34	10	32		Cochran (1981)

Table 1. (*Continued.*)

Lat. °N	Lon. °E	Datum	σ	Model	M.dir.	Reference
Arabia-Somalia: Transform azimuths (continued)						
12.32	47.86	33	10	33		Cochran (1981)
12.48	47.61	33	10	33		Cochran (1981)
12.35	47.02	34	10	33		Cochran (1981)
12.40	46.96	34	10	33		Cochran (1981)
12.21	46.53	34	10	34		Cochran (1981)
12.00	46.07	34	10	35		Cochran (1981)
12.13	45.61	28	10	35		Cochran (1981)
12.00	45.22	32	10	36		Cochran (1981)
12.00	44.91	33	10	36		Cochran (1981)
Arabia-Somalia: Slip vectors						
13.76	57.10	36	20	25		CMT 1.26.80
14.74	55.69	39	20	24		CMT 6.16.87
14.64	53.77	23	20	25		*CMT 7.8.79
14.29	51.82	28	15	27		*CMT 1.28.84
14.00	51.70	30	15	27		*Sykes (1970)
13.78	51.62	23	20	28		*CMT 12.22.79
13.66	51.06	27	15	28		CMT 9.14.90
13.13	50.94	36	15	29		CMT 12.17.77
12.83	48.55	37	15	31		CMT 11.24.89
12.66	48.11	43	20	32		CMT 5.23.86
Africa-Antarctica: Spreading rates						
-54.70	0.00	1.40	0.30	1.46	45	*Demets et al. (1990)
-54.00	4.00	1.40	0.40	1.48	45	*Demets et al. (1990)
-53.90	3.5	1.40	0.30	1.48	45	*Demets et al. (1990)
-52.20	14.50	1.60	0.30	1.55	35	*Norton (1976)
12.05	44.29	1.65	0.25	1.61	5	*Girdler et al. (1980)
Africa-Antarctica: Transform azimuths						
-54.44	1.70	45	5	47		Norton (1976)
-54.25	2.00	45	5	46		**Sclater et al. (1976)
-54.25	6.00	40	5	42		*Sclater et al. (1978)
-53.50	9.00	39	5	38		*Sclater et al. (1978)
-52.28	14.00	36	5	32		**Norton (1976)
-53.00	25.50	27	10	22		*DeMets et al. (1988)
Africa-Antarctica: Slip vectors						
-54.85	0.89	51	10	48		*CMT 5.22.78
-54.76	1.46	50	10	47		**CMT 3.29.85
-54.48	2.07	44	10	46		*CMT 12.18.78
-54.37	5.82	34	10	42		*CMT 11.17.79
-53.29	9.76	37	10	37		**CMT 1.5.86
-52.80	9.92	38	10	37		CMT 9.8.89
-52.75	11.28	38	10	35		CMT 9.8.89
-53.35	24.84	23	10	23		CMT 4.11.85
-52.49	25.89	20	10	21		CMT 9.1.83
Somalia-Antarctica: Spreading rates						
-44.70	36.20	1.50	0.40	1.64	15	*Bergh & Norton (1976)
-44.50	37.00	1.60	0.40	1.64	15	*Bergh & Norton (1976)
-44.20	38.50	1.60	0.30	1.64	15	*Bergh & Norton (1976)
-44.20	38.80	1.60	0.30	1.64	15	*Bergh & Norton (1976)
-43.30	39.50	1.60	0.30	1.64	15	*Bergh & Norton (1976)
-40.00	45.60	1.80	0.40	1.63	0	*Fisher & Sclater (1983)
-38.80	47.30	1.60	0.40	1.64	10	*Schlich & Patriat (1971)
-26.20	68.50	1.60	0.40	1.53	0	*Tapscott et al. (1980)
Somalia-Antarctica: Transform azimuths						
-46.29	35.00	18	5	15		Bergh & Norton (1976)
-46.00	35.15	17	5	15		Bergh & Norton (1976)
-45.50	35.20	15	5	15		*Fisher & Sclater (1983)
-44.30	38.20	16	10	13		*Bergh & Norton (1976)
-43.80	39.30	13	5	12		*Fisher & Sclater (1983)
-43.78	39.36	16	5	12		Bergh & Norton (1976)
-42.00	42.60	18	10	10		*Fisher & Sclater (1983)
-39.40	46.20	8	5	7		*Fisher & Sclater (1983)
-36.70	52.30	4	5	4		*Fisher & Sclater (1983)

Table 1. (*Continued.*)

Lat. °N	Lon. °E	Datum	σ	Model	M.dir.	Reference
Somalia-Antarctica: Transform azimuths (continued)						
-35.70	53.30	6	5	4		*Fisher & Sclater (1983)
-35.10	54.10	7	5	3		*Fisher & Sclater (1983)
-33.00	57.00	0	5	2		**Sclater et al. (1981)
-31.70	58.35	2	5	2		**Sclater et al. (1981)
-30.00	60.75	-6	10	0		**Sclater et al. (1981)
Somalia-Antarctica: Slip vectors						
-44.89	35.36	10	10	15		CMT 7.26.83
-43.39	38.67	14	10	12		CMT 6.13.89
-43.83	39.14	8	10	12		CMT 5.26.84
-43.21	39.49	14	10	12		CMT 6.13.89
-43.43	40.78	3	10	11		*Wald & Wallace (1986)
-43.21	41.99	8	10	10		**CMT 10.14.86
-39.23	46.07	11	10	8		CMT 2.19.89
-39.09	46.24	5	10	7		*CMT 3.12.79
-38.77	46.52	11	10	7		CMT 2.19.89
-36.43	52.42	-3	10	4		CMT 5.17.84
-36.08	53.51	4	10	3		**CMT 12.17.85
-36.46	53.54	3	10	3		CMT 5.17.84
-35.11	54.32	3	10	3		**CMT 12.24.85
-32.00	57.11	-5	10	2		*CMT 5.25.86
-32.64	57.48	6	10	2		*CMT 3.1.87

σ is the standard error assigned to a datum. Rates and their standard errors are listed in cm yr^{-1}. Azimuths and their standard errors are listed in degrees clockwise from north. M.dir. is the direction along which the spreading rate is measured, that is perpendicular to the ridge strike. Column 'Model' shows values computed using the four plates model of Table 4. Data with * are those used in NUVEL 1. ** indicates that the datum has been sightly changed with respect to NUVEL 1, taking into account the original reference or data file.

problem is given by

$$\sigma_M(\mathbf{m}) = \rho_M(\mathbf{m})\left[\frac{\rho_D(\mathbf{d})}{\mu_D(\mathbf{d})}\right]_{\mathbf{d}=f(\mathbf{m})} \quad (2)$$

where $\sigma_M(\mathbf{m})$ and $\rho_M(\mathbf{m})$ are *a posteriori* (i.e. the solution) and *a priori* probability densities over the model parameters, respectively. $\rho_D(\mathbf{d})$ is the probability density over the data set. $\mu_D(\mathbf{d})$ is the non-informative probability density over the data. Eq. (2) can be rewritten

$$\sigma_M(\mathbf{m}) = \rho_M(\mathbf{m})L(\mathbf{m}) \quad (3)$$

where $L(\mathbf{m})$ may be called the 'maximum likelihood' of the model $\mathbf{m}$. To use a Monte Carlo technique, $L(\mathbf{m})$ has to be computed as efficiently as possible to be able to iterate the computation a large number of times.

With the hypothesis of exponential errors on the data, the maximum likelihood can be expressed as follows:

$$L(\mathbf{m}) = \exp\left(-\sum_{i=1}^{n}\frac{|f^i(\mathbf{m}) - d^i_{obs}|}{\sigma^i_D}\right) \quad (4)$$

where d^i_{obs} are the observed data with (estimated) standard deviation σ^i_D, and n the number of data.

Misfit functions

The likelihood function (4) to be maximized is now discussed, because a large variety of misfit functions have been used by previous workers. The functions used by McKenzie & Sclater (1971) and Chase (1972) are not discussed as they do not weight the data according to their uncertainties. For the rates of motion, the expression $|f^i(\mathbf{m}) - d^i_{obs}|$ in eq. (4) represents the scalar difference between the observed rate and the projection of the predicted rate on the direction along which the rate is measured, i.e. perpendicular to the strike of the ridge (Chase 1972). Except for the fact that we use here the least absolute value criterion instead of the least-squares criterion, our misfit function for rates is identical to that of DeMets *et al.* (1990). For the directions of relative motion, Chase (1972) defined the misfit as the magnitude of the vector difference between the unit vectors parallel to the observed and predicted azimuths. DeMets *et al.* (1990) proposed to replace Chase's relation by an equivalent relation in terms of the sine of the half-angle between the observed and predicted directions. Minster *et al.* (1974) used a different fitting function for azimuths based on the Von Mises distribution of azimuths on a unit circle. Here the scalar difference (modulo π) between the observed and predicted azimuths is used as the measure of misfit (divided by the uncertainty σ^i) because it leads to similar results and speeds up the computation as it does not use trigonometric functions.

Putting the Monte Carlo method into practice

The *a priori* information is described by two sets of parameters: the data (spreading rates from magnetic anomalies, transform fault azimuths and slip vectors of earthquakes) and their associated uncertainties, and some *a priori* bounds on the rotation parameters (latitude, longitude, rate) which describe each independent rotation.

Note that if the *a priori* bounds are not properly chosen, there is a risk that the actual solution will be outside the searched parameter space. This can be easily avoided by running a first trial over the whole Earth.

A priori information on the model is described in the simplest way by a 'box car' function (Gaussian of infinite order). It consists for each of the R independent rotations (where $R = P - 1$ with P equal to the number of plates) of lower and upper bounds on the three parameters of the rotation vector. The *a priori* probability density $\rho_M(\mathbf{m})$ in eq. (3) is then a constant. In addition, the plate circuit should be specified for non-independent rotations.

The data set consists of N data points located on M plate boundaries. Each datum consists of its geographic coordinates and a value of azimuth (slip vector of the earthquake or transform fault) or of the relative velocity measured on a given direction (spreading rate; see Table 1). An estimated error is attributed to this datum. For the data included in NUVEL 1 the same errors were adopted, except for the slip vectors along the SWIR, for which the assigned errors (15–25°) are considered to be slightly overestimated in NUVEL 1. For all additional data, the errors were assigned according to our own estimates, generally 5° or 10° on the transform azimuths measured, 10–20° on the slip vectors, and 10–20 per cent on rates (Table 1). Note that these estimates were often shown to be pessimistic.

Note also that some plate boundaries may be less well documented than others, in spite of the existence of reliable data. This may happen simply because less ship-time has been devoted to some areas than others. Consequently, this set of information cannot be considered as corresponding to a random sampling of the plate boundary. For this reason, it appears desirable to weight each datum inversely to the number of data points on the corresponding boundary. This additional weight is to be added in eq. (4). This ensures that the solution is not biased by the larger body of information on some plate boundaries than on others.

Results of the inversion

Given this *a priori* information, eq. (4) is then easy to calculate for each randomly generated model. The computer program uses a pseudo-random generator to compute the model parameters used at each iteration. The minimum and maximum numbers of iterations, as well as a criterion for convergence, are chosen by the user. The convergence criterion is the stability of the computed 'mean model' over a given number of successive iterations. The 'mean model' is computed by the numerical integration of all previously generated models (see Tarantola 1987, for details). The computation is stopped when the space of the possible solutions is sufficiently explored—that is, when the 'mean model' remains stable (i.e. any further search in the model space would not significantly change the mean model). This procedure avoids falling into local minima.

The 'best fit' model retained is that maximizing the likelihood function eq. (4). In addition to the 'mean model', the covariance matrix is also computed by numerical integration. Error ellipses about each rotation pole may be then obtained by computing the eigenvalues and eigenvectors of the 2×2 matrix extracted from the covariance matrix. These error ellipses have a statistical meaning only if the probability density function $\sigma_M(\mathbf{m})$ is nearly Gaussian. Another way to obtain information about the uncertainties on the computed rotation parameters is to store all the models that fit the data within their uncertainties, and to plot them on a map instead of an error ellipse. In the following, the expression 'acceptable models' is used for these models. As the set of acceptable models strongly depends on the assigned errors (especially on very small errors, which would greatly shrink the range of acceptable models), it must be pointed out that this concept is not identical to that of confidence limits, but rather constitutes a guide for the search for best-fit solutions. This is especially useful when the uncertainties on the solution [i.e. the *a posteriori* probability density function over the model parameters $\sigma_M(\mathbf{m})$] is not Gaussian, which is found when the solution contains several local minima.

In addition, the computer program also gives some statistics on the data which allow the check that (1) the model parameters are well resolved by the data set (the *a posteriori* errors should be much smaller than the *a priori* bounds) and (2) that the *a priori* errors on the data were properly introduced. More details on the procedures will be given in a paper in preparation. In the following figures, the best-fitting Euler vectors as well as all the acceptable rotation poles, as defined here, are shown.

AFRICA, SOMALIA, ARABIA AND THE AFAR TRIPLE JUNCTION

Red Sea and the Levant Fault

Le Pichon & Gaulier (1988) have shown that the fit of magnetic anomaly 3 determined by Izzeldin (1982; 1987) between 19°N and 20°N results in a rotation pole (32°8'N, 23°E) which is fairly close to that determined by Garfunkel (1981) for the recent motion along the Levant Fault (32.8°N, 22.6°E). Le Pichon & Gaulier (1988) proposed that no (or negligible) motion now occurs in the Gulf of Suez, as further substantiated by the low seismic activity compared with that along the Levant Fault (Fig. 1), and that the kinematics of ARAB with respect to AFRI can be constrained by the motion along the Levant Fault, taking into account its leaky transform nature. The same conclusion was reached independently by Joffe & Garfunkel (1987), although, in their Table 4, they include the Sinai plate in their model, with a pole relative to AFRI (30.3°N, 28.1°E) close to the ARAB–AFRI pole (32.2°N, 24°E) and, of course, a much lower rotation rate (0.093°/Ma instead of 0.376°/Ma for ARAB–AFRI). However, in their Table 3, they assume that the Red Sea and Levant Fault poles coincide.

The ARAB–AFRI relative motion was determined using the trends of left-lateral strike-slip faults arranged *en échelon* within the Levant leaky transform zone (Garfunkel *et al.* 1981) and one slip rate along the Levant Fault, based on the lengths of active rhomb-grabens and the age of their sedimentary fill (Garfunkel *et al.* 1981), as well as four transform fault azimuths in the Red Sea (Izzeldin 1989), two slip vectors of earthquakes, and two spreading rates (Izzeldin 1987) (see Table 1).

The rotation obtained by inversion (32.62°N, 25.11°E, −0.499°/Ma) is in good agreement with that proposed by Le Pichon & Gaulier (1988) and Joffe & Garfunkel (1987) (Table 2 and Fig. 2). In fits well the observed rates and

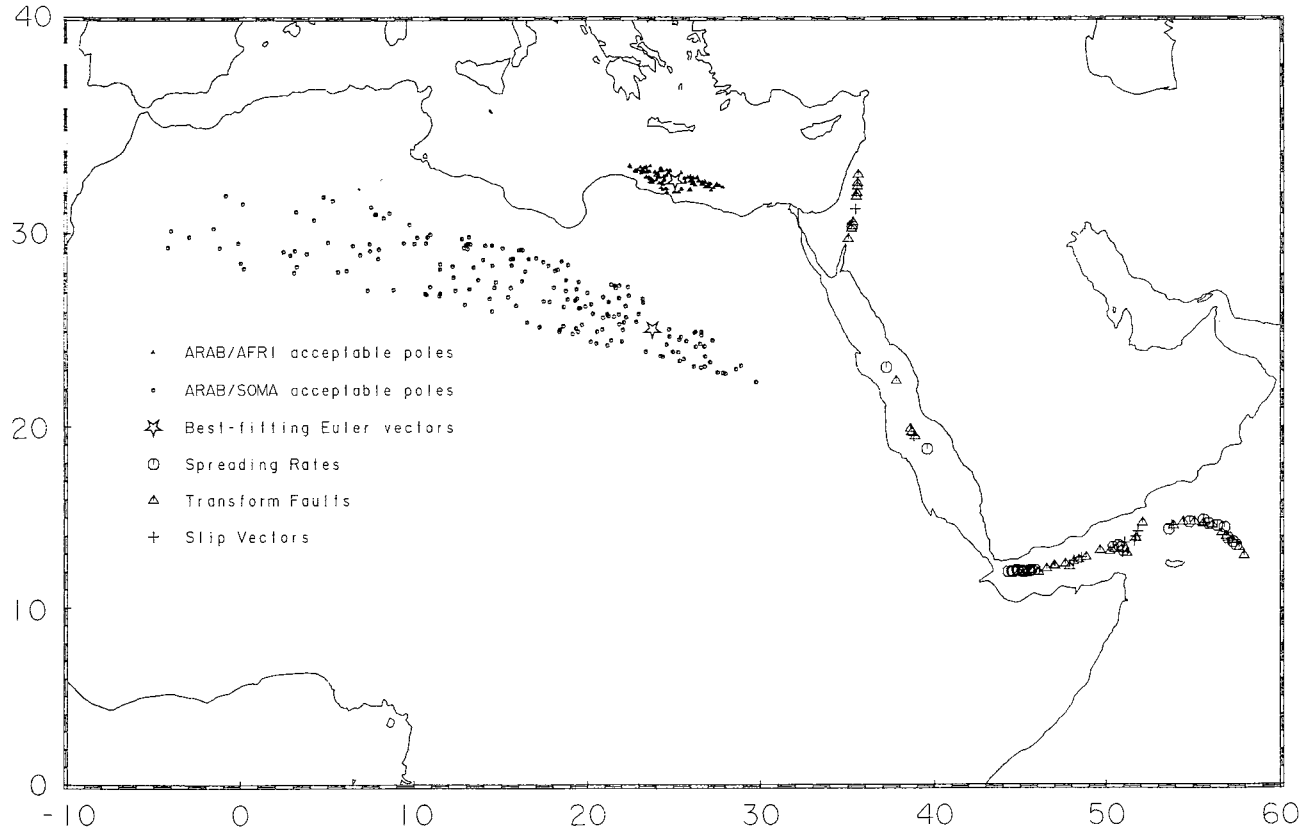

Figure 2. Two-plate kinematic analysis of the Red Sea and Gulf of Aden. The ARAB–AFRI and ARAB–SOMA best-fitting and acceptable rotation poles are shown, as well as the location of the data.

Table 2. Best-fitting ARAB–AFRI and ARAB–SOMA Euler vectors (rate is positive for clockwise rotation). SOMA–AFRI is computed by adding the two later vectors. Misfit is defined in text. Ref: reference (1, this work; 2, Garfunkel 1981; 3, Joffe & Garfunkel 1987; 4, Izzeldin 1982; 5, Le Pichon & Gaulier 1988; 6, DeMets *et al.* 1990 ARAB–AFRI best-fitting vector; 7, DeMets *et al.* 1990 ARAB–AFRI vector, NUVEL 1 global solution).

Plate pair	Euler vector			Misfit	Ref
	Latitude	Longitude	Rate °/Ma		
ARAB-AFRI	32.62°N	25.11°E	-0.499	0.217	1
	32.80°N	22.60°E	-	-	2
	32.20°N	24.00°E	-0.376	-	3
	32.80°N	22.60°E		-	4
	32.75°N	22.64°E	-0.402	-	5
ARAB-SOMA	25.20°N	23.74°E	-0.407	0.228	1
	25.00°N	26.00°E	-0.450	-	3
	23.80°N	23.40°E	-0.410	-	6
	24.10°N	24.00 °E	-0.420		7
SOMA-AFRI	61.08°S	145.31°W	0.109	-	1
	6.90°S	33.00°E	0.091	-	3

azimuths (Fig. 3), whereas the NUVEL 1 ARAB–AFRI rotation leads to large discrepancies, up to 0.4 cm yr^{-1}, for rates (as noted by DeMets *et al.* 1990) and as much as 40° for azimuths. The reason for these discrepancies is that the NUVEL 1 ARAB–AFRI motion is computed from data along the Gulf of Aden and thus is in fact the ARAB–SOMA motion.

Gulf of Aden

Data in the Gulf of Aden include many spreading rates from magnetic anomalies (Cochran 1981; Laughton, Whitmarsh & Jones 1970; Girdler *et al.* 1980; Tamsett & Girdler 1982), CMT earthquake slip vectors (Dziewonski and co-workers 1981 to 1991; Sipkin & Needham 1991), and transform fault

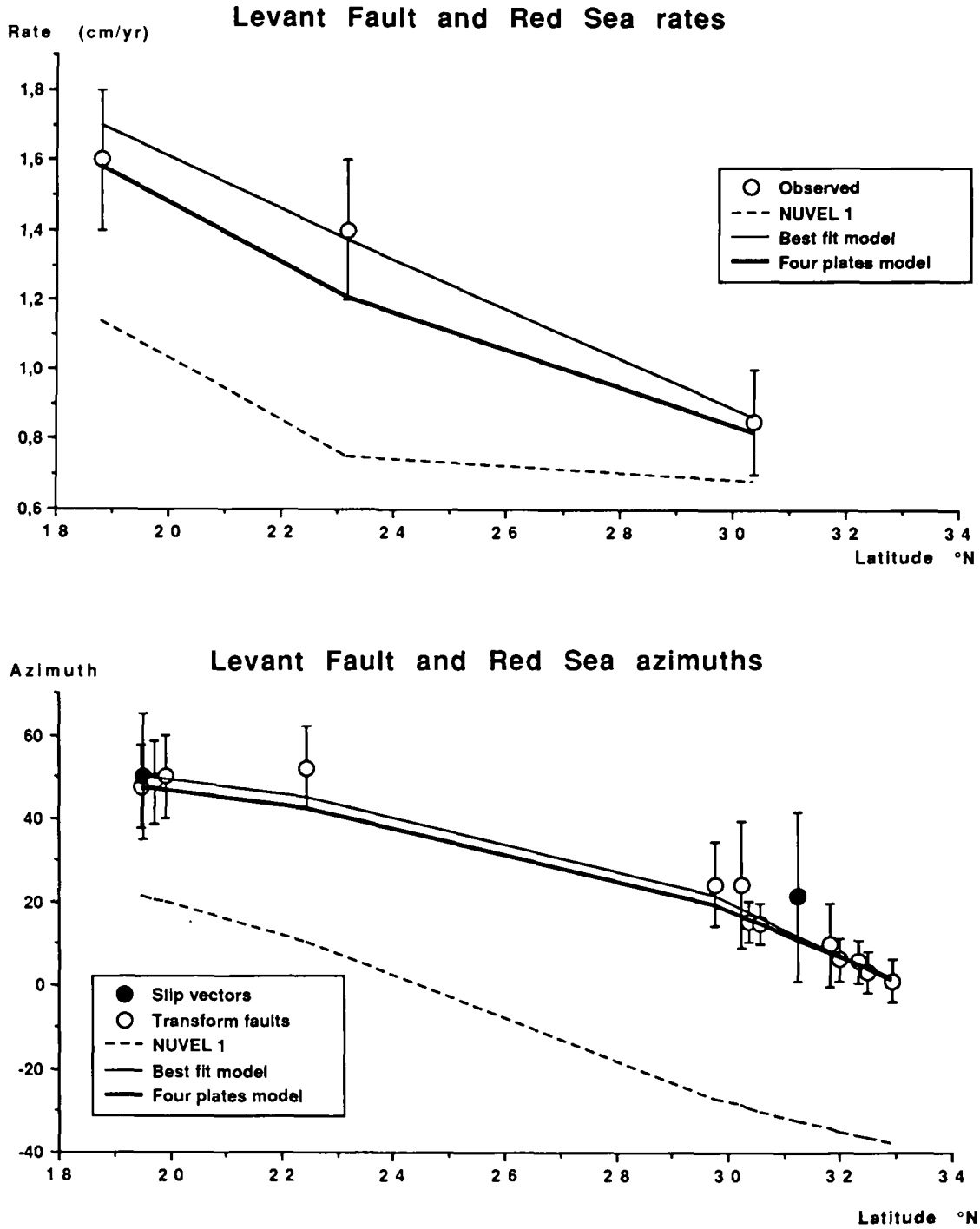

Figure 3. Comparison between observed rates (upper panel) and azimuths (lower panel) along the Levant Fault and the Red Sea and those computed from our ARAB–AFRI solutions (Tables 2 and 4). NUVEL 1 (global solution) ARAB–AFRI predicted rates and azimuths are shown for comparison.

azimuths deduced from the data of Cochran (1981). This data set is similar to that used in NUVEL 1 for the 'ARAB–AFRI' (in fact ARAB–SOMA) plate boundary, except for the transform fault azimuths. The three transform fault strikes from Gloria sidescan sonar (Tamsett & Searle 1988) used in NUVEL 1 were not taken into account because of the uncertainty in azimuth and their incoherence with those of Cochran (1981). Instead, 27 transform fault trends measured from Cochran's maps were used. The computed ARAB–SOMA pole of rotation is located at 25.20°N, 23.74°E, with a rotation rate of −0.407°/Ma (Table 2 and Fig. 2), very close to the ARAB–AFRI NUVEL 1 Euler vector, the difference arising from slightly different transform fault azimuths. The difference in predicted azimuths is only 2°, whereas the predicted rates differ only by 0.1 cm yr $^{-1}$ (Fig. 4).

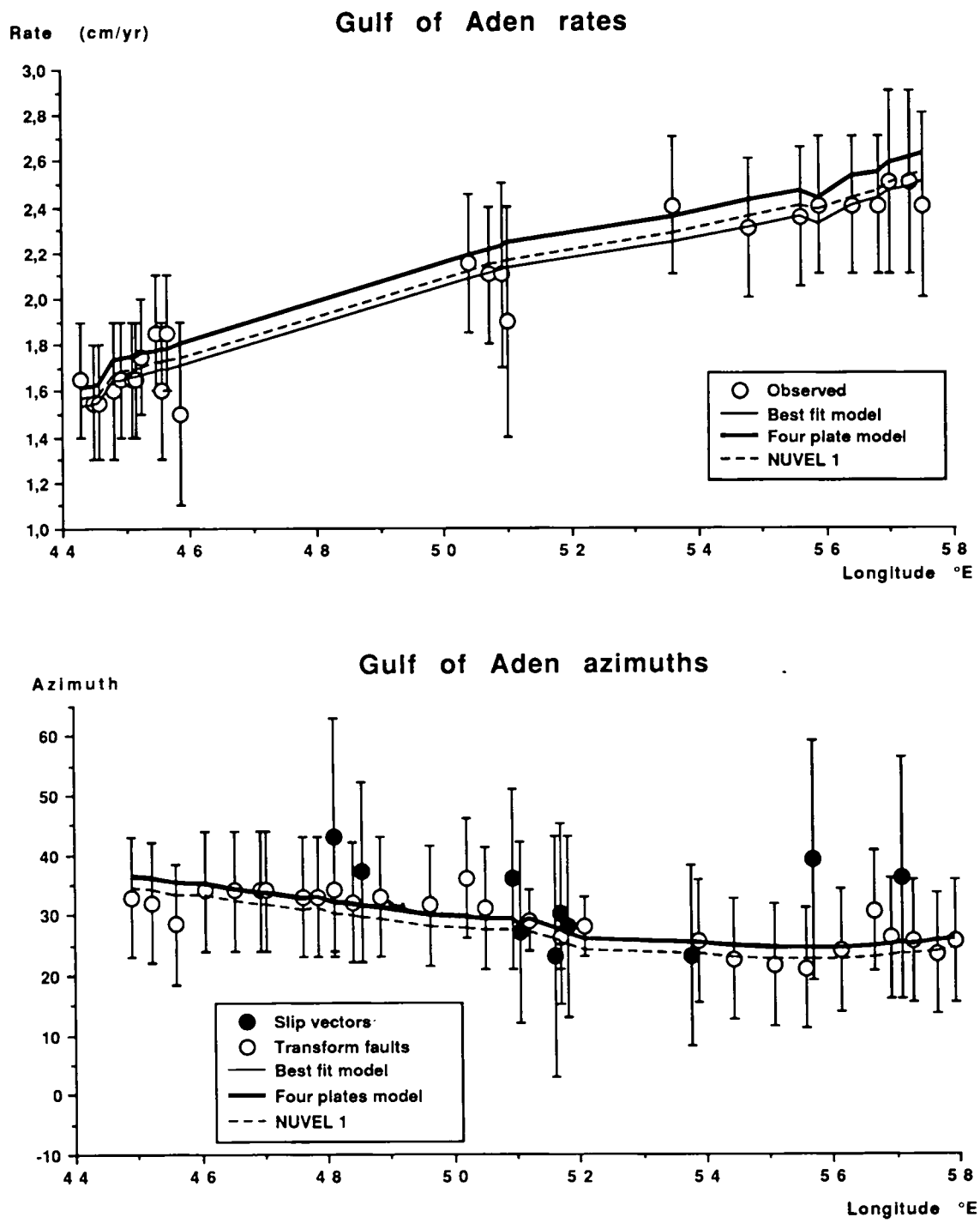

Figure 4. Comparison between observed rates (upper panel) and azimuths (lower panel) along the Gulf of Aden and those computed from our ARAB-SOMA solutions (Tables 2 and 4). NUVEL 1 (global solution) ARAB–AFRI predicted rates and azimuths are shown for comparison.

Consequences for the AFRI-SOMA relative motion

The two best-fitting Euler vectors, ARAB-SOMA and ARAB-AFRI, are thus clearly different. Furthermore, the acceptable rotation poles for the Red Sea and the Gulf of Aden do not overlap (Fig. 2). It is concluded that AFRI and SOMA can be treated as two distinct plates.

The SOMA–AFRI Euler vector obtained by summing the two previous ARAB–AFRI and ARAB-SOMA rotation poles is located at 61.08°S, 145.31°W, with a rotation rate of 0.109°/Ma (Table 2). Table 5 gives the predicted azimuths (087 and 090) for two points located along the EAR, which appear to be consistent with the nearly east–west extension across the EAR. Although they are not unreasonable, the computed rates (1.0 and 1.2 cm yr^{-1}) are too large compared with the rate of extension given by geodetic measurements (Mohr, Girnius & Rolff 1978). Remeasurement in 1992 of this geodetic network using the global

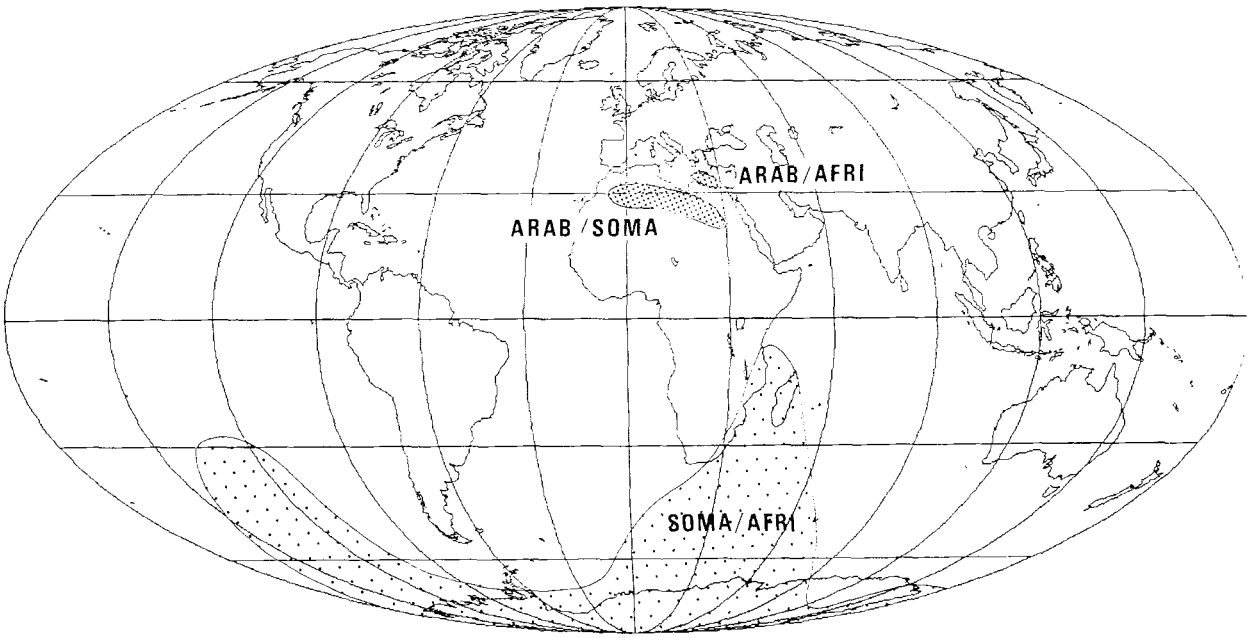

Figure 5. ARAB–AFRI, ARAB–SOMA and SOMA–AFRI acceptable poles, as defined in text (shaded areas).

positioning system led to a maximum widening rate of 1.1 ± 2.2 mm yr^{-1} (Asfaw *et al.* 1992). Meanwhile, the measured values may represent spatial or temporal quiescence and not be representative of the long-term motion across the EAR.

However, with respect to the ARAB–AFRI and ARAB–SOMA poles, being very close to each other, any small change either in the location of the pole of rotation or in the rotation rate results in a dramatic change in the AFRI–SOMA Euler vector. Fig. 5 shows the AFRI–SOMA poles resulting from the addition of any combination of acceptable ARAB–AFRI and ARAB–SOMA rotation vectors. These AFRI–SOMA poles are approximately located on a portion of a great circle in the prolongation of the Ethiopian Rift between latitudes 10°S and 90°S (Fig. 5). Although all compatible with the overall east–west extension along the EAR, the resulting SOMA–AFRI Euler vectors are clearly poorly constrained.

THE 'TRIPLE JUNCTION' AFRI–SOMA–ANTA

It was shown in the preceding section that an AFRI–SOMA plate boundary is required to explain the kinematics of the Red Sea and Gulf of Aden, which form, with the EAR, the Afar triple junction. It is suggested that the whole EAR system can be considered as the AFRI–SOMA plate boundary. This boundary should then intersect another plate boundary to the south, most likely the SWIR. However, such a hypothetical AFRI–SOMA–ANTA triple junction, at the intersection between the SWIR and the EAR, is expressed neither by seismicity nor by bathymetry. The reason for this absence of geophysical evidence is clear considering the location of the AFRI–SOMA pole of rotation, which leads to no or negligible motion near the AFRI–SOMA–ANTA triple junction. However, the consistency between the SOMA–AFRI relative motion as determined in the previous section and the relative motion along the SWIR needs to be checked.

Transform faults and slip vectors along the SWIR

When compiling available data along the SWIR, slight differences were found between a few slip vectors used in NUVEL 1 and the original data file or reference. These data are mostly CMT slip vectors, taken from the Harvard CMT digital data file. The difference between our data and those in NUVEL 1 is, however, very small (no more than a few kilometres in location, mainly because earthquake locations from the Harvard digital data file were used here, while NUVEL 1 generally refers to Dziewonski's publications). A few transform fault azimuths were added from Norton (1976) and Bergh & Norton (1976), which were not included in NUVEL 1. As already mentioned, the errors assigned to slip vector data taken from NUVEL 1 were reduced because we think that they are overestimated, leading to a small influence of these data in the solution, as shown by the small data importance for this plate boundary (see Table 3 in Demets *et al.* 1990).

The transform azimuth data were checked with the new marine gravity map of Sandwell & Smith (1992), based on SeaSat, GeoSat and ERS-1 data, and no discrepancy between the azimuth data listed in Table 1 and the azimuths measured on the map was found. All the available data between longitudes 25°E and 35°E are omitted to avoid possible perturbations due to the proximity of the diffuse triple junction. Therefore, the data set is separated into two groups (Table 1), one between the Bouvet triple junction and the Mozambique Ridge, which corresponds to the AFRI–ANTA plate boundary, and the other between the Mozambique Ridge and the Rodriguez triple junction (SOMA–ANTA plate boundary).

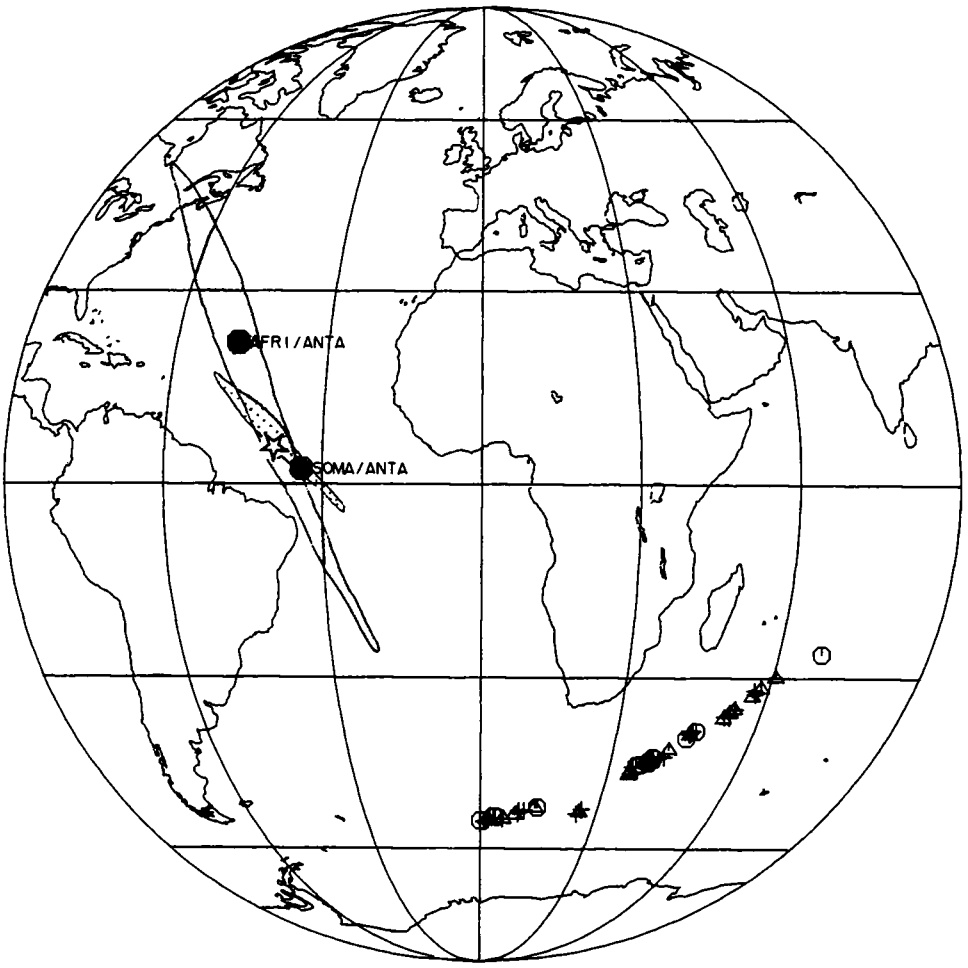

Figure 6. Two-plate kinematic analysis along the SWIR. AFRI–ANTA and SOMA–ANTA best-fitting (dots) and acceptable rotation poles (shaded area) are shown, as well as the NUVEL 1 AFRI–ANTA pole (star) and location of data (caption: see Fig. 2).

Computed AFRI–ANTA and SOMA–ANTA relative motions

Data from the SWIR were inverted in the same way as data for the Red Sea and Gulf of Aden, obtaining Euler vectors for the individual plate boundaries AFRI–ANTA and SOMA–ANTA. Although the AFRI–ANTA and SOMA–ANTA best-fit Euler vectors are different (Fig. 6 and Table 3), the two areas of acceptable AFRI–ANTA and SOMA–ANTA rotation poles overlap (Fig. 6). We thus confirm that the data along the SWIR can be fitted with a single Euler vector, as shown previously by DeMets *et al.* (1988). This is further demonstrated by the fact that the NUVEL 1 AFRI–ANTA pole lies at the intersection of these two areas (Fig. 6).

Examination of the observed and computed rates and azimuths (Fig. 7) shows that our three plate solution leads to results similar to those of the two plate NUVEL 1 solution

Table 3. Best-fitting ANTA–AFRI and ANTA–SOMA Euler vectors (rate is positive for clockwise rotation). SOMA–AFRI is computed by adding the two later vectors. Ref: reference (1, this work; 2, DeMets *et al.* 1990 ANTA–AFRI best-fitting vector; 3, DeMets *et al.* 1990 ANTA–AFRI vector, NUVEL 1 global solution).

Plate pair	Euler vector			Misfit	Ref
	Latitude	Longitude	Rate °/Ma		
ANTA-AFRI	13.82°N	43.55°W	-0.128	0.229	1
	6.00 °N	39.30 °W	-0.140	0.304	2
	5.60°N	39.20 °W	-0.130	0.358	3
ANTA-SOMA	2.39°N	33.86°W	0.146	0.297	1
SOMA-AFRI	38.38°S	8.67°E	0.040	-	-

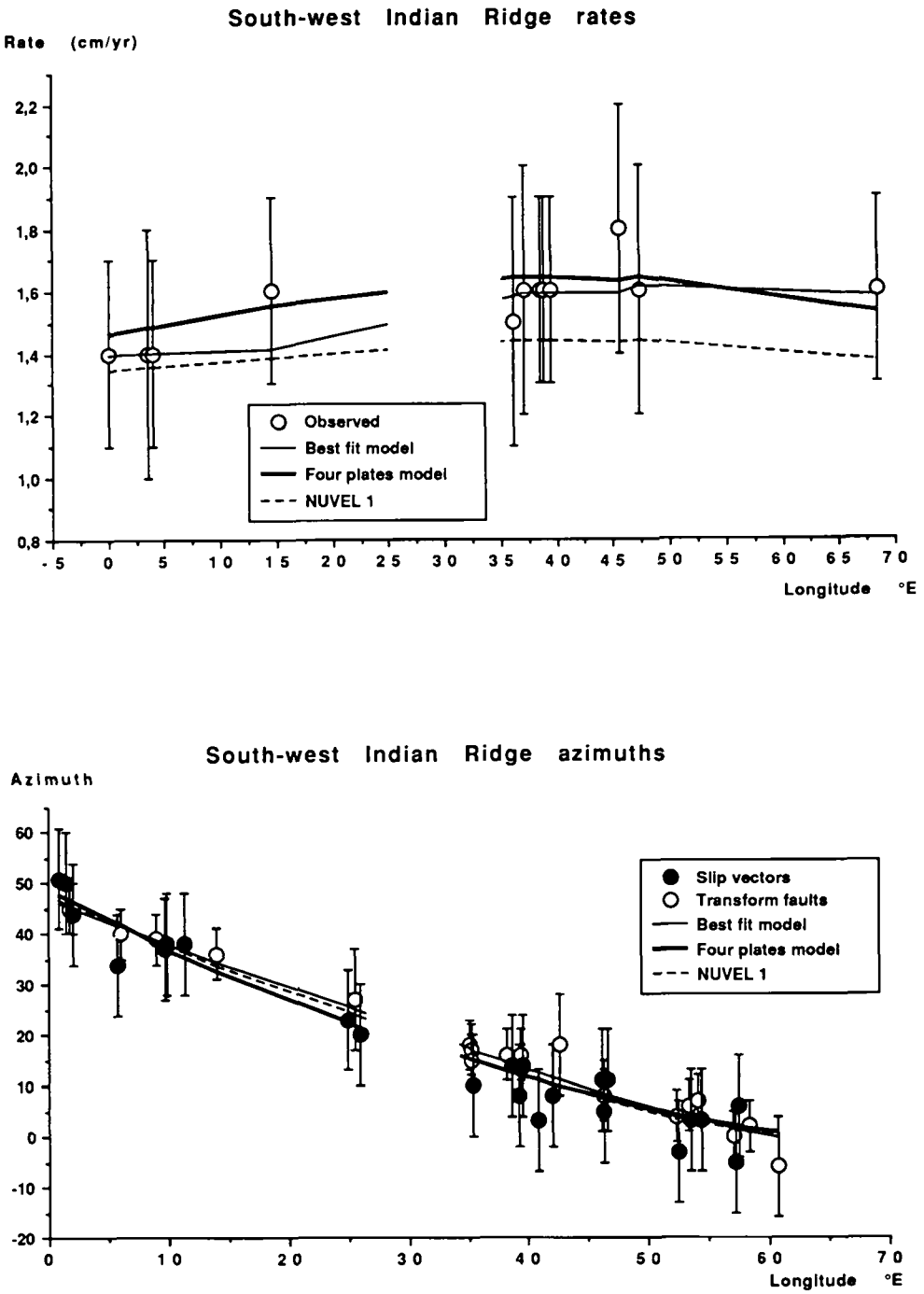

Figure 7. Comparison between observed rates (upper panel) and azimuths (lower panel) along the SWIR and those computed from our AFRI–ANTA and SOMA–ANTA solutions (Tables 3 and 4). NUVEL 1 (global solution) AFRI–ANTA predicted rates and azimuths are shown for comparison.

in terms of azimuths (Fig. 7b), but fits the rates better (Fig. 7a) because, as noted by DeMets *et al.* (1990), the NUVEL 1 predicted rates are systematically too low. This is reflected by the fact that the normalized misfits (in the least absolute value sense) obtained for AFRI–ANTA and SOMA–ANTA (0.229 and 0.297, respectively; see Table 3) are slightly smaller than the misfit obtained with the NUVEL 1 best solution (0.304) or the global solution (0.358). It was further checked that the data set along the SWIR does not pass the F test as defined by Stein & Gordon (1984), as the computed value of $F(2.28)$ is smaller than the F value at the 95 per cent risk level (2.78). Thus, as shown by DeMets *et al.* (1988), the occurrence of two plates north of the SWIR cannot be assessed from the available data along the SWIR alone. This is confirmed when all the SOMA–AFRI Euler vectors resulting from the combination of the AFRI–ANTA

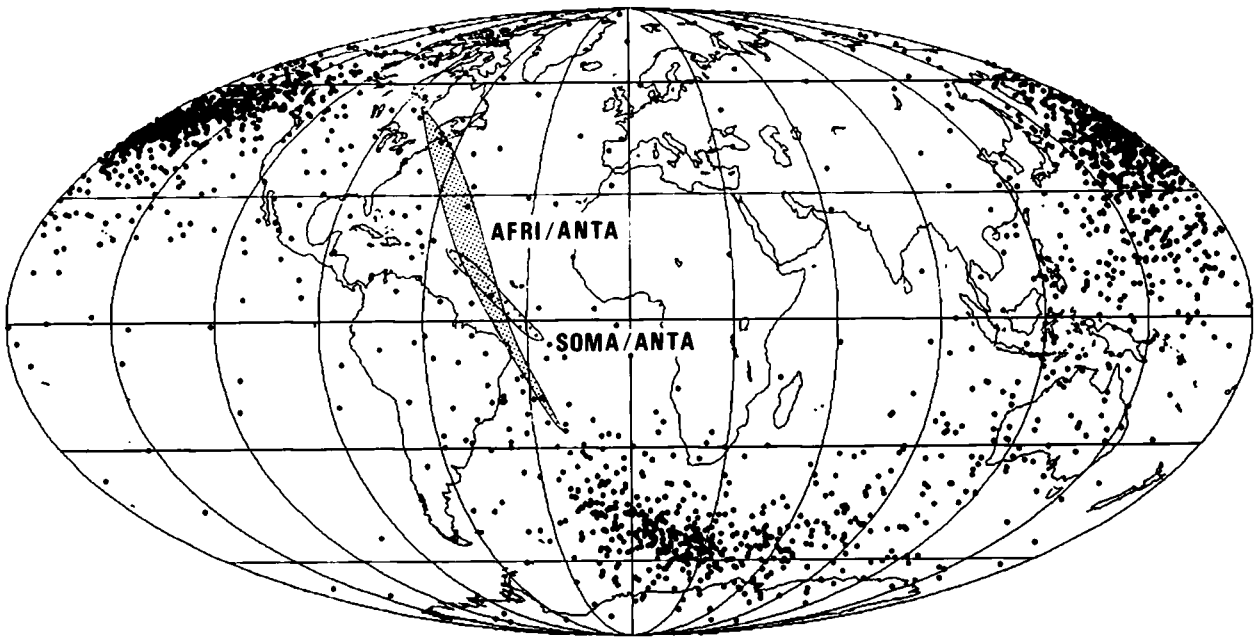

Figure 8. AFRI–ANTA and SOMA–ANTA acceptable poles, as defined in text (shaded areas). Positions of possible SOMA–AFRI poles are shown as dots.

and SOMA–ANTA acceptable poles are computed. The possible SOMA–AFRI poles are dispersed over almost the whole Earth (Fig. 8).

RESOLVING THE AFRI–SOMA RELATIVE MOTION

The previous analysis suggests that the only way to better resolve the motion along the EAR is to perform a simultaneous inversion of data in the Red Sea, Gulf of Aden and along the SWIR. The AFRI–SOMA Euler vector will then be determined simultaneously by the closure of the ARAB–AFRI–SOMA and AFRI–ANTA–SOMA plate circuits. The results of this inversion (Table 4) show, as expected, only small changes in the ARAB–AFRI, ARAB–SOMA, AFRI–ANTA and SOMA–ANTA Euler vectors, whereas the area of possible SOMA–AFRI rotation poles is drastically reduced (Fig. 9). Figs 3, 4 and 7 show that the differences in predicted rates and azimuths along the Red Sea, the Gulf of Aden and the SWIR, with respect to the previous two-plate analyses, is almost negligible. The SOMA–AFRI best-fit vector obtained (55.73°S, 19.76°E, 0.054°/Ma) is located close to the diffuse SWIR–EAR triple junction, in agreement with the previous analysis.

The solution derived here is different from that proposed by Chase (1978) (71.10°S, 144.60°W, 0.060°/Ma), although it is also compatible with east–west extension along the EAR. Note that the pole of Chase (1978) predicts a maximum in the rate of relative motion along the EAR near 20°S, which is contradictory to the lack of seismicity and clearly defined geological structures south of latitude 25°S. In addition, it was found that the pole of Chase (1978) is incompatible with data along the SWIR. Although the uncertainty is still large (Fig. 9), the AFRI–SOMA rotation pole derived here appears to be better constrained than in previous kinematic models. Moreover, the introduction of this AFRI–SOMA rotation requires only minor changes in the rotations of neighbouring plates. Thus the solution derived here is probably consistent with NUVEL 1, which means that NUVEL 1 only has to be adjusted within its uncertainties to fit in the proposed AFRI–SOMA motion, although this remains to be tested further.

Table 4. Best-fitting ARAB–AFRI, ARAB–SOMA, ANTA–AFRI and ANTA–SOMA Euler vectors (rate is positive for clockwise rotation). SOMA–AFRI is constrained by simultaneous closure around the ARAB–AFRI–SOMA and AFRI–SOMA–ANTA triple junction.

Plate pair	Euler vector			Misfit
	Latitude	Longitude	Rate °/Ma	
ARAB-AFRI	32.59°N	23.70°E	-0.418	0.306
ARAB-SOMA	25.24°N	23.39°E	-0.423	0.282
ANTA-AFRI	8.67°S	32.00°W	0.165	0.282
ANTA-SOMA	7.70°N	41.41°W	0.148	0.345
SOMA-AFRI	55.73°S	19.76°E	0.054	-

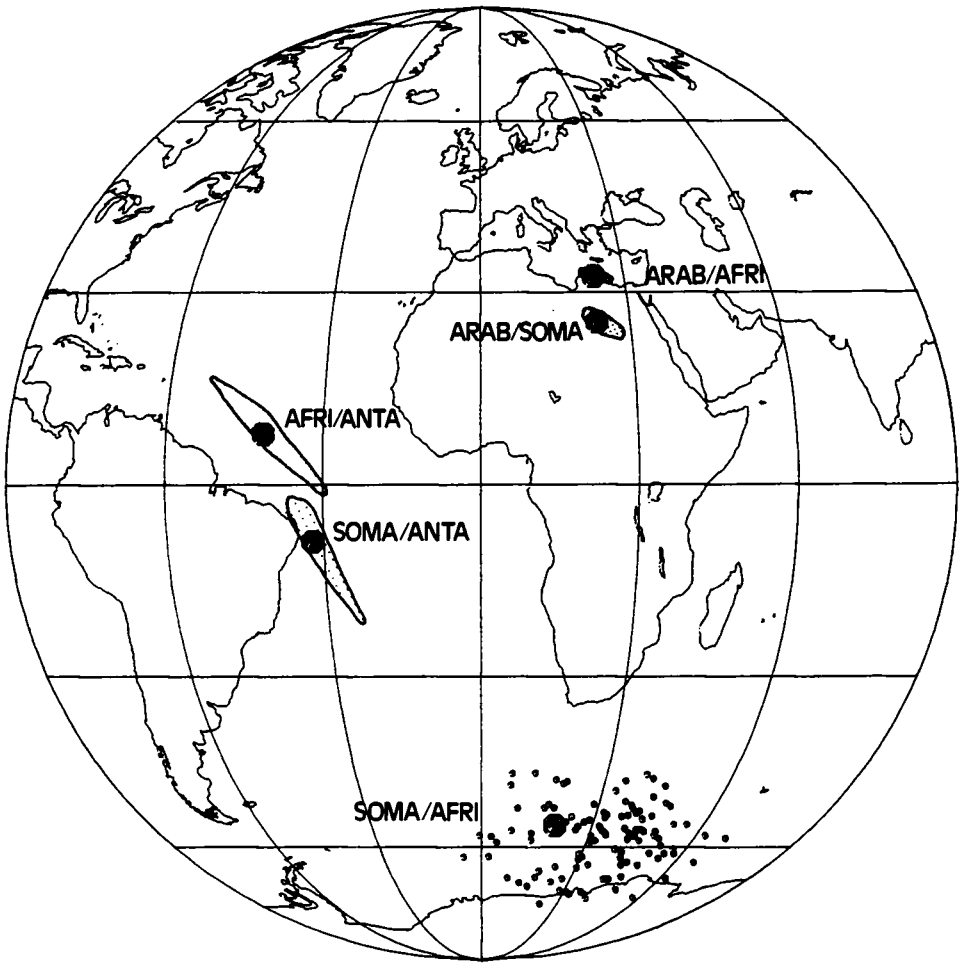

Figure 9. Four plate solution (see Table 4). Shaded areas show the acceptable rotation poles, as defined in text. Positions of possible SOMA–AFRI poles are shown as dots.

DISCUSSION

AFRI–SOMA kinematics and the stress pattern over the EAR

The predictions of this model, which has been obtained without any constraint from the EAR itself, are now compared with the pattern of deformation along the EAR. The only place where the EAR displays a localized deformation is its northern extremity, close to the Afar triple junction. Available slip vectors of earthquakes in this area (Fig. 10) show an average N100°E trend, whereas the value predicted with the pole derived here is N102°E (Table 6), which is well within the error bars. Microtectonic studies at the northernmost extremity of the EAR also indicates a nearly east–west direction of extension during the Quaternary (Gaulier & Huchon 1991). In the main part of the EAR, the deformation is widely distributed, even if most of it occurs along the two branches of the EAR (Fig. 10). Borehole breakout data in Kenya (eastern EAR) indicates an average N125°E trend of the least horizontal stress direction, in good agreement with the trend of aligned Quaternary volcanic vents (Bosworth, Strecker & Blisniuk 1992). Microtectonic studies of the Gregory rift also indicate an east–west to NW–SE direction of extension (Strecker, Blisniuk & Elsbacher 1990). Further north, detailed tectonic mapping of the rift shows a N110°E direction of extension (Hackman *et al.* 1990). Tectonic data in the Malawi and

Table 5. Azimuths and rates at both ends of the EAR computed with previous SOMA–AFRI Euler vectors.

SOMA-AFRI Euler vector	Point 1 (9°N,40°E)		Point 2 (20°S,34°E)	
	Azimuth	Rate cm/yr	Azimuth	Rate cm/yr
from table 2	087	1.0	090	1.2
from table 3	120	0.4	134	0.2
from table 4	102	0.5	103	0.4

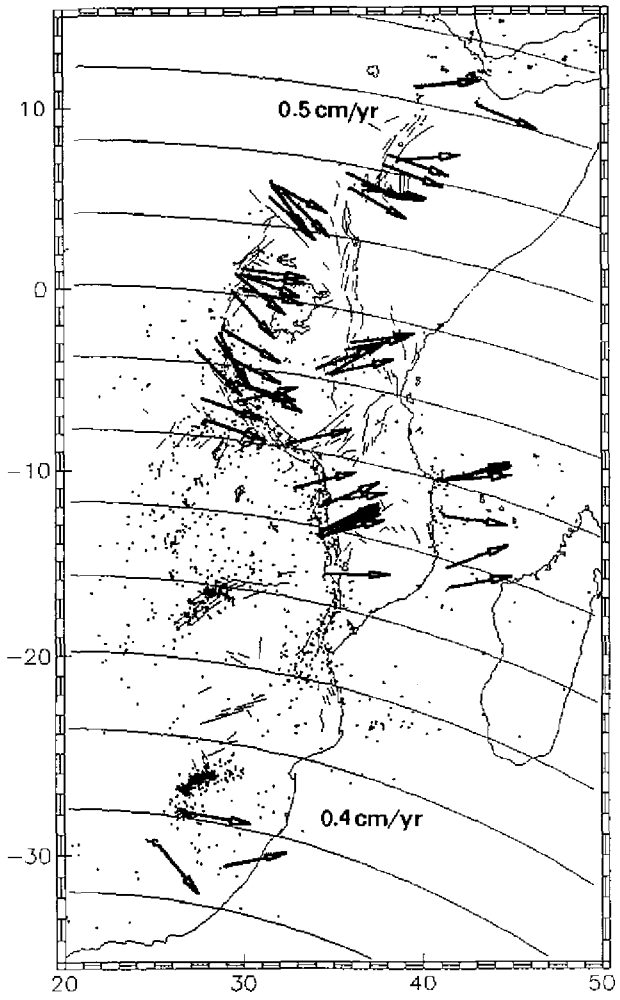

Figure 10. Main tectonic features (from Chorowicz & Sorlien 1992), seismicity and earthquake slip vectors [from CMT catalogues; Shudovsky (1985) and Grimison & Chen (1988)] along the EAR compared with small circles around our SOMA–AFRI solution (Table 4).

Tanganyika Rifts (western EAR) also indicate a WNW–ESE to NW–SE direction of extension (Chorowicz & Sorlien 1992; Scott, Etheridge & Rosendahl 1992). All these data are thus in fairly good agreement with the direction of plate separation inferred from our model. Near 5°S, the eastern branch of the EAR disappears, but part of the relative motion is probably transferred to the Kerimbas graben and Davie ridge, between the African coast and Madagascar (Mougenot *et al.* 1986), where a north–south trending swarm of earthquakes occurs, with east–west trending slip vectors (Fig. 10). Further south, few earthquake data are available.

As mentioned earlier and well demonstrated by the pattern of seismicity (Fig. 1), the deformation along the EAR seems to be distributed on several rifts separated by nearly undeformed small blocks. The most individualized block is the 'Victoria' block (from Lake Victoria), which is located between the eastern and western branches of the EAR. Fig. 10 shows the small circles centred around our SOMA–AFRI pole, superimposed on available slip vectors of earthquakes. Note that the mean trend of slip vectors on the western rift is approximately N130°E and is thus clearly different from the mean direction of motion along the eastern rift (about N90°E), as well as along the Davie Ridge. It is thus impossible to use these data together for directly computing the SOMA–AFRI rotation pole. A possible solution would be to separate these data in two parts and to compute two different Euler vectors for the two AFRI–Victoria and Victoria–SOMA plate boundaries. Unfortunately, reliable results were not obtained, as data along the EAR are too scarce to obtain sufficiently constrained rotation poles. Moreover, a lack of information about the distribution of rates between the two rifts prevents any control on the kinematic solution in term of rates.

Predicted and observed rates of motion along the EAR

Estimating the present-day rate of extension along the EAR is especially difficult because the rate is very low. As discussed earlier, the geodetically determined rates in the Ethiopian rift range from 1 (Asfaw *et al.* 1992) to 5 mm yr^{-1} (Mohr *et al.* 1978). The total amount of extension is also difficult to determine from geological or geophysical data. Based on vertical offsets along the border faults of the Kivu–Rusizi Rift (western branch of the EAR), Ebinger (1989) proposes a maximum east–west crustal extension of 16 km. Considering that the rift was mostly active since 5 Ma (Davidson & Rex 1980) leads to a rate of about 3 mm yr^{-1}, a value which falls within the range of geodetically determined rates. At the northern end of the EAR, this model predicts a value of 5 mm yr^{-1} (Table 5), which is

Table 6. Comparison between observed slip vectors in the northern part of the EAR and azimuths computed from the SOMA–AFRI rotation vector in this work (four plates solution, see Table 4).

Lat. °N	Lon. °E	Observed	Computed	Reference
7.35	38.16	110	101	CMT 6.8.89
7.03	38.60	85	102	CMT 12.2.83
6.80	37.85	110	101	CMT 6.8.89
6.35	35.88	115	100	CMT 10.7.87
5.72	36.69	105	101	CMT 10.28.87
5.41	36.73	97	101	CMT 10.25.87
-11.80	34.46	83	102	CMT 9.5.89
-15.72	34.59	91	102	Shudofsky (1985)

reasonable considering the uncertainties in the AFRI–SOMA motion.

Southward continuation of the EAR

As noted earlier, seismicity associated with the two branches of the EAR disappears south of latitude 22°S (Fig. 1). However, diffuse seismicity still exists to the south, but does not seem to be associated with rift structures (Kebede & Kulhànek 1991). Based on hypocentres relocation and fault plane solution determination, Grimison & Chen (1988) proposed that the southern termination of the AFRI–SOMA plate boundary is a diffuse zone of east–west extension up to 2000 km wide. An extensive discussion about the southern continuation of the EAR is made by Hartnady (1990), who proposes that the EAR is presently propagating southwards, the propagator tip now being located in the Lesotho–Natal area (30°S, 28°E), where the seismicity map reveals a swarm of earthquakes (Fig. 10). It might then follow the break-up of the northern Mozambique basin down to the SWIR near 40°E, where unusually large magnitude earthquakes have occurred (Hartnady 1990). As also noted by Hartnady, the extensional focal mechanisms of earthquakes around the Urema graben (20°S, 34°E; see Fig. 10) are not in agreement with the AFRI–SOMA pole of rotation at 17.5°S, 31.9°E given by Woods *et al.* (1985), which predicts convergence instead of extension. Based on NUVEL 1 and seismic slip vectors from Shudofsky (1985), Shudofsky *et al.* (1987) have shown that the AFRI–SOMA rotation pole should be well to the south of Africa, a conclusion also reached here, but without using any constraints on the EAR.

This analysis has shown that it is now possible to include explicitly the SOMA plate in a *regional* kinematic model without any major changes in the global kinematic parameters along the Gulf of Aden and the SWIR. In addition, these revised SOMA–AFRI parameters now provide some constraints on the kinematic boundary conditions around the Afar triple junction as well as along the EAR diffuse deformation zone.

ACKNOWLEDGMENTS

This work was initiated by X. Le Pichon during his lectures at the Collège de France. Advice by N. Chamot-Rooke and G. Marquis is gratefully acknowledged. A. Tarantola convinced us of the usefulness of considering a Bayesian approach to the inverse problem. This work also benefited from the constructive remarks of two anonymous reviewers, who helped to significantly improve the manuscript. CNRS-INSU-DBT contributions No. 621. Laboratoire de Géologie de l'ENS contribution No. 270.

REFERENCES

Asfaw, L. M., Bilham, R., Jackson, M. & Mohr, P., 1992. Recent inactivity in African rift, *Nature*, **357**, 447.

Bergh, H. W. & Norton, I. O., 1976. Prince Edward Fracture Zone and the evolution of the Mozambique basin, *J. geophys. Res.*, **81**, 5221–5239.

Bosworth, W., Strecker, M. R. & Blisniuk, P. M., 1992. Integration of East African paleostress and present-day stress data: implications for continental stress field dynamics, *J. geophys. Res.*, **97**, 11 851–11 865.

Chase, C. G., 1972. The *N*-plate problem of plate tectonics, *Geophys. J. R. astr. Soc.*, **29**, 117–122.

Chase, C. G., 1978. Plate kinematics: the Americas, East Africa and the rest of the world, *Earth planet. Sci. Lett.*, **37**, 355–368.

Chorowicz, J. & Sorlien, C., 1992. Oblique extensional tectonics in the Malawi rift, Africa, *Geol. Soc. Am. Bull.*, **104**, 1015–1023.

Cochran, J. R., 1981. The gulf of Aden: structure and evolution of a young ocean basin and continental margin, *J. geophys. Res.*, **86**, 263–287.

Davidson, A. & Rex, D. C., 1980. Age of volcanism and rifting in southwestern Ethiopia, *Nature*, **283**, 657–658.

DeMets, C., Gordon, R. G. & Argus, D. F., 1988. Intraplate deformation and closure of the Australia–Antarctica–Africa plate circuit, *J. geophys. Res.*, **93**, 11 877–11 897.

DeMets, C., Gordon, R. G., Argus, D. F. & Stein, S., 1990. Current plate motions, *Geophys. J. Int.*, **101**, 425–478.

Dziewonski, A. M., Chou, T. A. & Woodhouse, J. H., 1981. Determination of earthquake source parameters from waveform data for studies of global and regional seismicity, *J. geophys. Res.*, **86**, 2825–2852.

Dziewonski, A. M., Friedman, A. & Woodhouse, J. H., 1983a. Centroid-moment tensor solutions for January–March 1983, *Phys. Earth planet. Inter.*, **33**, 71–75.

Dziewonski, A. M., Friedman, A., Giardini, D. & Woodhouse, J. H., 1983b. Global seismicity of 1982: centroid-moment tensor solutions for 308 earthquakes, *Phys. Earth planet. Inter.*, **33**, 76–90.

Dziewonski, A. M., Franzen, J. E. & Woodhouse, J. H., 1984a. Centroid-moment tensor solutions for July–September 1983, *Phys. Earth planet. Inter.*, **34**, 1–8.

Dziewonski, A. M., Franzen, J. E. & Woodhouse, J. H., 1984b. Centroid-moment tensor solutions for October–December 1983, *Phys. Earth planet. Inter.*, **34**, 129–136.

Dziewonski, A. M., Francen, J. E. & Woodhouse, J. H., 1984c. Centroid-moment tensor solutions for January–March 1984, *Phys. Earth planet. Inter.*, **34**, 209–219.

Dziewonski, A. M., Franzen, J. E. & Woodhouse, J. H., 1985a. Centroid-moment tensor solutions for April–June 1984, *Phys. Earth planet. Inter.*, **37**, 87–96.

Dziewonski, A. M., Franzen, J. E. & Woodhouse, J. H., 1985b. Centroid-moment tensor solutions for July–September 1984, *Phys. Earth planet. Inter.*, **39**, 147–156.

Dziewonski, A. M., Franzen, J. E. & Woodhouse, J. H., 1985c. Centroid-moment tensor solutions for October–December 1984, *Phys. Earth planet. Inter.*, **37**, 87–96.

Dziewonski, A. M., Franzen, J. E. & Woodhouse, J. H., 1985d. Centroid-moment tensor solutions for January–March 1985, *Phys. Earth planet. Inter.*, **40**, 249–258.

Dziewonski, A. M., Franzen, J. E. & Woodhouse, J. H., 1986a. Centroid-moment tensor solutions for April–June 1985, *Phys. Earth planet. Inter.*, **41**, 215–224.

Dziewonski, A. M., Franzen, J. E. & Woodhouse, J. H., 1986b. Centroid-moment tensor solutions for July–September 1985, *Phys. Earth planet. Inter.*, **42**, 205–214.

Dziewonski, A. M., Franzen, J. E. & Woodhouse, J. H., 1986c. Centroid-moment tensor solutions for October–December 1985, *Phys. Earth planet. Inter.*, **43**, 185–195.

Dziewonski, A. M., Ekström, G., Franzen, J. E. & Woodhouse, J. H., 1987a. Global seismicity of 1977: centroid-moment tensor solutions for 471 earthquakes, *Phys. Earth planet. Inter.*, **45**, 11–36.

Dziewonski, A. M., Ekström, G., Franzen, J. E. & Woodhouse, J. H., 1987b. Global seismicity of 1978: centroid-moment tensor solutions for 512 earthquakes, *Phys. Earth planet. Inter.*, **46**, 316–342.

Dziewonski, A. M., Ekström, G., Franzen, J. E. & Woodhouse, J.

H., 1987c. Global seismicity of 1979: centroid-moment tensor solutions for 524 earthquakes, *Phys. Earth planet. Inter.*, **48,** 18–46.

Dziewonski, A. M., Ekström, G., Franzen, J. E. & Woodhouse, J. H., 1987d. Centroid-moment tensor solutions for January–March 1986, *Phys. Earth planet. Inter.*, **45,** 1–10.

Dziewonski, A. M., Ekström, G., Franzen, J. E. & Woodhouse, J. H., 1987e. Centroid-moment tensor solutions for April–June 1986, *Phys. Earth planet. Inter.*, **45,** 229–39.

Dziewonski, A. M., Ekström, G., Franzen, J. E. & Woodhouse, J. H., 1987f. Centroid-moment tensor solutions for July–September 1986, *Phys. Earth planet. Inter.*, **46,** 305–315.

Dziewonski, A. M., Ekström, G., Woodhouse, J. H. & Zwart, G., 1987g. Centroid-moment tensor solutions for October–December 1986, *Phys. Earth planet. Inter.*, **48,** 5–17.

Dziewonski, A. M., Ekström, G., Franzen, J. E. & Woodhouse, J. H., 1988a. Global seismicity of 1980: centroid-moment tensor solutions for 515 earthquakes, *Phys. Earth planet. Inter.*, **50,** 127–154.

Dziewonski, A. M., Ekström, G., Franzen, J. E. & Woodhouse, J. H., 1988b. Global seismicity of 1981: centroid-moment tensor solutions for 542 earthquakes, *Phys. Earth planet. Inter.*, **50,** 155–182.

Dziewonski, A. M., Ekström, G., Woodhouse, J. H. & Zwart, G., 1988c. Centroid-moment tensor solutions for January–March 1987, *Phys. Earth planet. Inter.*, **50,** 116–126.

Dziewonski, A. M., Ekström, G., Woodhouse, J. H. & Zwart, G., 1988d. Centroid-moment tensor solutions for April–June 1987, *Phys. Earth planet. Inter.*, **50,** 215–225.

Dziewonski, A. M., Ekström, G., Woodhouse, J. H. & Zwart, G., 1989. Centroid-moment tensor solutions for October–December 1987, *Phys. Earth planet. Inter.*, **54,** 10–21.

Dziewonski, A. M., Ekström, G., Woodhouse, J. H. & Zwart, G., 1990a. Centroid-moment tensor solutions for January–March 1989, *Phys. Earth planet. Inter.*, **59,** 233–242.

Dziewonski, A. M., Ekström, G., Woodhouse, J. H. & Zwart, G., 1990b. Centroid-moment tensor solutions for April–June 1989, *Phys. Earth planet. Inter.*, **60,** 243–253.

Dziewonski, A. M., Ekström, G., Woodhouse, J. H. & Zwart, G., 1990c. Centroid-moment tensor solutions for July–September 1989, *Phys. Earth planet. Inter.*, **62,** 185–193.

Dziewonski, A. M., Ekström, G., Woodhouse, J. H. & Zwart, G., 1990d. Centroid-moment tensor solutions for October–December 1989, *Phys. Earth planet. Inter.*, **62,** 193–207.

Dziewonski, A. M., Ekström, G., Woodhouse, J. H. & Zwart, G., 1991a. Centroid-moment tensor solutions for January–March 1990, *Phys. Earth planet. Inter.*, **65,** 197–206.

Dziewonski, A. M., Ekström, G., Woodhouse, J. H. & Zwart, G., 1991b. Centroid-moment tensor solutions for April–June 1990, *Phys. Earth planet. Inter.*, **66,** 133–143.

Dziewonski, A. M., Ekström, G., Woodhouse, J. H. & Zwart, G., 1991c. Centroid-moment tensor solutions for July–September 1990, *Phys. Earth planet. Inter.*, **67,** 211–220.

Ebinger, C. J., 1989. Geometric and kinematic development of border faults and accommodation zones, Kivu–Rusizi rift, Africa, *Tectonics,* **8,** 117–133.

Fisher, R. L. & Sclater, J. G., 1983. Tectonic evolution of the Southwest Indian Ocean since the Mid-Cretaceous: plate motions and stability of the pole of Antarctica–Africa for at least 80 Myr, *Geophys. J. R. astr. Soc.*, **73,** 553–576.

Forsyth, D. W., 1975. Fault plane solutions and tectonics of the South Atlantic and Scotia Sea, *J. geophys. Res.*, **80,** 1429–1443.

Garfunkel, Z., 1981. Internal structure of the Dead Sea leaky transform (rift) in relation to plate kinematics, *Tectonophysics,* **80,** 81–108.

Garfunkel, Z., Zak, I. & Freund, R., 1981. Active faulting in the Dead Sea Rift, *Tectonophysics,* **80,** 1–26.

Gaulier, J. M. & Huchon, P., 1991. Tectonic evolution of Afar triple junction, *Bull. Soc. géol. France,* **162,** 451–464.

Girdler, R. W., Brown, C., Noy, D. J. M. & Styles, P., 1980. A geophysical survey of the westernmost Gulf of Aden, *Phil. Trans. R. Soc. Lond.*, A, **298,** 1–43.

Gordon, R. G. & DeMets, C., 1989. Present-day motion along the Owen Fracture Zone and Dalrymple Trough in the Arabian Sea, *J. geophys. Res.*, **94,** 5560–5570.

Gordon, R. G., DeMets, C. & Argus, D. F., 1990. Kinematic constraints on distributed lithospheric deformation in the equatorial Indian ocean from present motion between the Australian and Indian plates, *Tectonics,* **9,** 409–422.

Gregory, J. W., 1921. *The Rift Valleys and Geology of East Africa,* Seely Service, London.

Grimison, N. L. & Chen, W. P., 1988. Earthqakes in the Davie Ridge–Madagascar region and the Southern Nubian–Somalian plate boundary, *J. geophys. Res.*, **93,** 10 439–10 450.

Hackman, B. D., Charsley, T. J., Key, R. M. & Wilkinson, A. F., 1990. The development of the East African rift system in north-central Kenya, *Tectonophysics,* **184,** 189–211.

Harland, W. B., Cox, A. V., Llewellyn, P. G., Pickton, C. A. G., Smith, A. G. & Walters R., 1982. *A Geologic Time Scale,* Cambridge University Press, Cambridge.

Hartnady, C. J. H., 1990. Seismicity and plate boundary evolution in southeastern Africa, *S. Afr. J. Geol.*, **93,** 473–484.

Huang, P. Y. & Solomon, S. C., 1987. Centroid depth and mechanisms of mid-ocean ridge earthquakes in the Indian ocean, Gulf of Aden and Red Sea, *J. geophys. Res.*, **92,** 1361–1382.

Izzeldin, A. Y., 1987. Seismic, gravity and magnetic surveys in the central part of the Red Sea: their interpretation and implications for the structure and evolution of the Red Sea, *Tectonophysics,* **143,** 269–306.

Izzeldin, A. Y., 1989. Transverse structures in the central part of the Red Sea and implications for the early stages of oceanic accretion, *Geophys. J.*, **96,** 117–129.

Jestin, F. & Huchon, P., 1992. Cinématique et déformation de la jonction triple Mer Rouge–Golfe d'Aden–Rift Ethiopien depuis l'Oligocène, *Bull. Soc. géol. France,* **163,** 125–133.

Joffe, S. & Garfunkel, Z., 1987. Plate kinematics of the circum Red Sea—a re-evaluation, *Tectonophysics,* **141,** 5–22.

Kebede, F. & Kulhànek, O., 1991. Recent seismicity of the East African rift system and its implications, *Phys. Earth planet. Inter.*, **68,** 259–273.

Laughton, A. S., Whitmarsh, R. B. & Jones, M. T., 1970. The evolution of the gulf of Aden, *Phil. Trans. R. Soc. Lond.*, A, **267,** 227–266.

Le Pichon, X., 1968. Sea-floor spreading and continental drift, *J. geophys. Res.*, **73,** 3661–3697.

Le Pichon, X. & Francheteau, J., 1978. A plate tectonic analysis of the Red Sea–Gulf of Aden area, *Tectonophysics,* **46,** 369–406.

Le Pichon, X. & Gaulier, J. M., 1988. The rotation of Arabia and the Levant fault system, *Tectonophysics,* **153,** 271–294.

McKenzie, D. P. & Morgan, W. J., 1969. Evolution of triple junctions, *Nature,* **224,** 125–133.

McKenzie, D. P. & Sclater, J. G., 1971. The evolution of the Indian Ocean since the late Cretaceous, *Geophys. J. R. astr. Soc.*, **25,** 437–528.

McKenzie, D. P., Davies, D. & Molnar, P., 1970. Plate tectonics of the Red Sea and East Africa, *Nature,* **226,** 243–248.

Minster, J. B. & Jordan, T. H., 1978. Present day plate motions, *J. geophys. Res.*, **83,** 5331–5354.

Minster, J. B., Jordan, T. H., Molnar, P. & Haines, E., 1974. Numerical modelling of instantaneous plate tectonics, *Geophys. J. R. astr. Soc.*, **36,** 541–576.

Mohr, P., Girnius, A. & Rolff, J., 1978. Present-day strain rates at the northern end of the Ethiopian Rift valley, *Tectonophysics,* **44,** 141–160.

Mougenot, D., Recq, M., Virlogeux, P. & Lepvrier, C., 1986. Seaward extension of the East African Rift, *Nature,* **331,** 599–603.

Norton, I. O., 1976. The present relative motion between Africa and Antarctica, *Earth planet. Sci. Lett.,* **33,** 219–230.

Sandwell, D. T. & Smith, W. H. F., 1992. Global marine gravity from ERS-1, Geosat and Seasat reveals new tectonic fabric *EOS, Trans. Am. geophys. Un.,* **73,** 43–133.

Schlich, R. & Patriat, P., 1971. Mise en évidence d'anomalies magnétiques axiales sur la branche ouest de la dorsle médio-indienne, *C. R. Acad. Sci. Paris,* **272,** 700–703.

Sclater, J. G., Bowin, C., Hey, R., Hoskins, H., Peirce, J., Phillips, J. & Tapscott, C., 1976. The Bouvet triple junction, *J. geophys. Res.,* **81,** 1857–1869.

Sclater, J. G., Dick, H., Norton, I. O. & Woodroffe, D., 1978. Tectonic structure and petrology of the Antarctic plate boundary near the Bouvet triple junction, *Earth planet. Sci. Lett.,* **37,** 393–400.

Sclater, J. G., Fisher, R. L., Patriat, P., Tapscott, C. & Parsons, B., 1981. Eocene to recent development of the Southwest Indian ridge, a consequence of the evolution of the Indian Ocean triple junction, *Geophys. J. R. astr. Soc.,* **64,** 587–604.

Scott, D. L., Etheridge, M. A. & Rosendahl, B. R. 1992. Oblique-slip deformation in extensional terrains: a case study of the lakes Tangakyina and Malawi rift zones, *Tectonics,* **11,** 998–1009.

Shudofsky, G. N., 1985. Source mechanisms and focal depths of East African earthquakes using Rayleigh-wave inversion and body-wave modelling, *Geophys. J. R. astr. Soc.,* **83,** 563–614.

Shudofsky, G. N., Cloetingh, S., Stein, S. & Wortel, R., 1987. Unusually deep earthquakes in East Africa: constraints on the thermo-mechanical structure of a continental rift system, *Geophys. Res. Lett.,* **14,** 741–744.

Sipkin, S. A. & Needham, R. E., 1991. Moment-tensor solutions estimated using optimal filter theory: global seismicity, 1988–1989, *Phys. Earth planet. Inter.,* **67,** 221–230.

Stein, S. & Gordon, R. G., 1984. Statistical tests of additional plate boundaries from plate motion inversions, *Earth planet. Sci. Lett.,* **69,** 401–412.

Strecker, M. R., Blisniuk, P. M. & Eisbacher, G. H., 1990. Rotation of extension direction in the central Kenyan rift, *Geology,* **18,** 299–302.

Sykes, L. R., 1970. Focal mechanism solutions for earthquakes along the world rift system, *Bull. seism. Soc. Am.,* **60,** 1749–1752.

Tamsett, D. & Girdler, R. W., 1982. Gulf of Aden axial magnetic anomaly and the Curie temperature isotherm, *Nature,* **298,** 149–151.

Tamsett, D. & Searle, R. C., 1988. Structure and development of the mid-ocean ridge plate boundary in the Gulf of Aden: evidence from GLORIA side scan sonar, *J. geophys. Res.,* **94,** 3157–3178.

Tapscott, C., Patriat, P., Fisher, R. L., Sclater, J. G., Hoskins, H. & Parsons, B., 1980. The Indian Ocean triple junction, *J. geophys. Res.,* **85,** 4723–4739.

Tarantola, A., 1987. *Inverse Problem Theory,* Elsevier, Amsterdam.

Tarantola, A. & Valette, B., 1982. Inverse problems = quest for information, *J. Geophys.,* **50,** 159–170.

Wald, D. J. & Wallace, T. C., 1986. A seismically active segment of the Southwest Indian Ridge, *Geophys. Res. Lett.,* **13,** 1003–1006.

Woods, D. F., Quibel, D., DeMets, C., Gordon, R. G., Stein, S., Argus, D., Lundgren, P., Stein, C. A., Weinstein, S. A., Engeln, J. & Wiens, D., 1985. Constraints on Nubia-Somalia rifting from NUVEL 1 relative plate motion data, *Trans. Am. geophys. Un.,* **66,** 1062.